Study of Single Gold Nanocrystals by Inelastic Light Scattering Spectroscopy

Mariana Timm, Lucien Saviot, Aurélien Crut, Nicholas Blanchard, Lucian Roiban, Karine Masenelli-Varlot, Lucile Joly-Pottuz, Jérémie Margueritat

Study of Single Gold Nanocrystals by Inelastic Light Scattering Spectroscopy

Mariana M. Timm[1,2,*], Lucien Saviot[3], Aurélien Crut[2], Nicholas Blanchard[2], Lucian Roiban[1], Karine Masenelli-Varlot[1], Lucile Joly-Pottuz[1], and Jérémie Margueritat[2,*]

[1]*Univ-Lyon, INSA, UCBL, CNRS, MATEIS UMR 5510, 69621 Villeurbanne, France*

[2]*Institut Lumière Matière, UMR5306, Université Lyon 1-CNRS, Université de Lyon, 69622 Villeurbanne, France*

[3]*Laboratoire Interdisciplinaire Carnot de Bourgogne, UMR 6303 CNRS-Université de Bourgogne Franche Comté, 9 Avenue A. Savary, BP 47 870, F-21078 Dijon Cedex, France*

*corresponding author: mariana.de-mello-timm@insa-lyon.fr and jeremie.margueritat@univ-lyon.fr

Abstract. Optical spectroscopy techniques represent a powerful tool to study the vibrational modes of nano-objects and address both their intrinsic properties (related to nanoparticle morphology, crystallinity, and local environment) and their interaction with light, which plays a key role for nanophotonics and optomechanics applications. In this paper, we report low-frequency inelastic light scattering measurements on single gold nanocrystals, combined with detailed characterizations of their morphology and environment using transmission electron microscopy and tomography, and numerical simulations of their optical and vibrational responses. Our studies confirm the conclusions of previous ensemble measurements regarding the large impact of the nanoparticle crystallinity on inelastic scattering spectra. Moreover, their single-particle character allows us to address subtle shape and environment effects. We show that slight nanoparticle shape anisotropies induce further splitting of Raman-active modes. We also demonstrate that local environment anisotropies lead to richer inelastic light scattering spectra and allow the detection of vibrational modes predicted to be Raman-inactive by usual Raman selection rules, which are based on the (here invalid) assumption of a symmetric internal electric field.

1. Introduction

The small dimensions of nano-objects are at the origin of the appearance of original optical properties resulting from the confinement of excitons in semiconductor nanoparticles and the localised surface plasmons in metallic ones.[1,2] The latter are now widely used in many applications thanks to the recent development of fabrication and characterization techniques paving the way for nano-plasmonic engineering linking both the intrinsic plasmonic

properties of individual particles and their interactions with their environment or each other.[3,4] More recently, it has been shown that there is a strong interaction between the plasmonic and vibrational (mechanical) properties of nano-objects that can be used to develop nano-optomechanics based on metal nanoparticles.[5–7] However, while the control of the plasmonic properties tends to be a mature technology, the control of the vibrational properties of nano-objects and their assembly and their interaction with light are in their infancy. Following the example of developments in the field of plasmonics, the tools for measuring the acoustic vibrations of nano-objects are evolving and allow to constantly improve our understanding of the mechanisms involved in light-vibration interactions in nano-objects (not necessarily metallic) and thus to envisage the joint engineering of the acoustic and optical properties of nanoparticles.

The acoustic vibrations of nanoparticles are controlled by their size,[8–10] shape,[11–13] crystallinity,[14] composition,[15,16] and environment.[17–19] These dependencies have mostly been investigated using optical methods operating in the time or frequency domains. Among these, inelastic light scattering spectroscopy relies on the interaction of monochromatic light with some of the vibrational modes of the nanoparticles,[20] which allows an accurate measurement of their frequency.[21,22] Since the early 1990s, a large number of low-frequency Raman spectroscopy studies have been carried out to investigate the acoustic vibrations of nanoparticles.[23–26] Initial investigations were mainly conducted on nanosphere assemblies, and interpreted in the framework of Lamb theory, developed at the end of the 19th century to model the vibrations of an elastically isotropic sphere.[27] Although this theory is based on continuum mechanics, it has been shown to correctly describe the vibrations of spherical nanoparticles, even for diameters as small as 1 nm.[28,29] Lamb theory classifies vibration modes into torsional and spheroidal categories, and indexes them with l and n integers (angular momentum and radial numbers). Their associated frequencies can be written as $\nu_{\ell,n} = S_{\ell,n} v_{L,T}/D$, where $S_{\ell,n}$ is a dimensionless proportionality factor depending on the considered vibrational mode, $v_{L,T}$ is the velocity of sound (longitudinal or transverse) in the material, and D is the diameter of the particle.[30] However, these vibrational modes do not all scatter light inelastically. In the case of object shapes presenting symmetries, group theory assigns an irreducible representation to each mode allowing to predict which ones are Raman-active, based on selection rules obtained by assuming a uniform internal electric field inside the nanoparticles. When applied to elastically isotropic nanospheres, this approach predicts that all torsional modes are Raman-inactive and that, among the spheroidal ones, only $l = 0$

(breathing) and $l = 2$ (quadrupolar) modes are Raman-active.[20] Experiments on glass-embedded metal nanospheres have confirmed the validity of these selection rules and shown that the fundamental $l = 2$ quadrupolar mode is usually dominant.[31] This mode presents a $2* l + 1 = 5$ degeneracy for an elastically isotropic sphere (the situation considered by the Lamb model). This degeneracy is partly lifted for nanoparticles whose shape presents a lower symmetry (e.g. when considering ellipsoidal shapes instead of spherical ones),[29,32] or for nanospheres with crystalline anisotropy (as crystallinity leads to different sound velocities for acoustic phonons propagating along different crystallographic directions).[33] As a result of these effects, the quadrupolar mode of an elastically isotropic sphere may split into up to five modes for nanoparticles with more anisotropic shapes and/or elasticities. For example, it splits into two distinct modes with E_g and T_{2g} irreducible representations for nanospheres with cubic crystallinity (e.g., monocrystalline gold nanospheres).[33] The frequencies and displacement fields associated to the vibrational modes of nanoparticles with non-spherical shape and/or crystalline anisotropy can be calculated using numerical methods and assigned to a point group symmetry. The experimental frequencies of detected modes are generally in agreement with computed ones. However, determining which vibrational modes are Raman-active is more challenging as usual selection rules, which rely on the assumption of a uniform electric field in the nanoparticles (well verified only for small nanospheres located in a homogeneous environment), may be misleading in the case of nanoparticles with non-spherical shapes or surrounded by an inhomogeneous environment.[34] Furthermore, our recent work has demonstrated that an inhomogeneity of the internal electric field induced by the presence of a neighbouring nanoparticle allows the observation of light scattering by vibration modes which are undetectable in the case of well-separated nanoparticles.[35,36] Tracking the appearance of new features in the inelastic light scattering spectra of nanoparticles is therefore a way to follow the change of the internal electric field induced by a modification of their environment.

Most previous inelastic light scattering studies have been carried out on assemblies of nanoparticles. In this case, the measured inelastic spectra are affected by the size, shape, crystallinity and orientation distributions of the nanoparticles being investigated, as well as by their acoustic and optical interactions, which typically lead to an inhomogeneous broadening of the peaks. An effective way to overcome these spurious effects is to perform vibrational investigations on single particles. This approach has now become standard in the field of time-resolved spectroscopy,[37–39] but has only been recently introduced in the context of Raman spectroscopy.[34,36] High-resolution electron energy loss spectroscopy (EELS) has also been recently used to map the vibrational modes in single MgO structures,[40] allowing the 3D

reconstruction of the phononic surface electromagnetic fields.[41] Although this technique achieves unprecedented spatial resolution, its implementation is time-consuming and it cannot be easily applied to the systematic studies of nanoparticle vibrations.

We report here ultra-low-frequency Raman spectroscopy measurements on single monocrystalline Au nanoparticles with cuboidal shapes, supported on a thin silica membrane, complemented by extensive characterizations of their morphology and crystallinity by electron microscopy and tomography and theoretical modelling of their vibrational and optical properties. The results described in this paper were obtained on four distinct nanoparticles: two well-isolated ones with different shapes (referred to as NPr and NPc), and two other ones (NPcs and NPrs) very similar to NPr and NPc in terms of shape but located near a step of the silica substrate supporting them, making their environment more anisotropic (the indices "r" and "c" stand for round and cubic, and "s" for step).

2. Materials and Methods

The PVP-coated, cubic shaped gold nanoparticles with a nominal edge size of 100 nm used in this work were purchased from Nanopartz (Loveland, CO, USA). A 5 µL drop of the commercial solution diluted 100 times in water was deposited on a 40 nm thick SiO_2 TEM membrane and left to dry for several minutes. This procedure allows for a distribution of particles generally separated by at least 2 µm from each other. The position of each particle of interest on the SiO_2 film was initially identified by low-magnification TEM (see **Figure S2** in Supporting Information).

2.1 Low-frequency Raman Spectroscopy

The sample was positioned on a capacitive piezo-electric translation stage placed above the objective lens of an inverted optical microscope with an entrance connected to a solid-state laser (λ = 660 nm, filtered with a TABAL temperature filter) and an exit connected to a Brillouin spectrometer (Tandem Fabry-Perot from JRS Scientific Instruments). The laser light was focused on the sample with the objective lens (x100) with a NA = 0.95 numerical aperture. The position of the individual particles was retrieved by confocal mapping (**Figure S3**), with a laser power of 100 µW. Low-frequency Raman spectroscopy was performed at the single-particle level, with a laser power of 20 mW. A light power of about 0.4 mW at the level of the sample was used, allowing long measurements (2 to 6 hours) without damaging the particles, as confirmed by TEM observations performed before and after the inelastic light scattering measurements. The experiments reported here were measured within the spectral

range of -22.5 to 22.5 GHz. A rotator of polarization was used to investigate the influence of polarization of incident light on the inelastic light scattering spectra of the nanoparticles. To avoid the risk of sample degradation due to the long acquisition time, measurements were performed using only three different polarization angles for each nanoparticle. Note that the crystalline orientation of the nanoparticles in relation to the polarization angles was not known at this stage of the experiments. The experimental configuration is schematically shown in **Figure S1**.

2.2 Transmission Electron Microscopy and Electron Tomography

After the low-frequency measurements on the chosen particles, the size, shape, and crystallinity of the particles were characterized with TEM and Selected Area Electron Diffraction (SAED), using a JEOL 2100 microscope operating at 200 kV.

Electron Tomography was performed to have an accurate measure of the three dimensions of the particles. Initially, 5 nm gold nanoparticles were deposited on the SiO_2 grid to serve as fiducial markers for the alignment step. Electron tomography was carried out with a high tilt sample holder using a spherical aberration (Cs) corrected ThermoFischer Titan ETEM (80-300 keV)microscope operating at 300 kV in the STEM-HAADF mode in high vacuum. The acquisition of tilt series was done semi-automatically using the electron tomography plugin of the TIA software, which controls the tilting step by step with a 2º increment. The defocusing and specimen drift were adjusted manually. The recorded images of the tilted series were aligned using the IMOD software.[42] The volume reconstruction was done using 15 interactions of the OS-ART algorithm[43] implemented via the TomoJ plugin[44] working in the ImageJ software. Finally, segmentation and quantification were performed with ImageJ tools[45] and 3D Slicer.[46]

The x and y lengths (Table 1) of the particles were extracted from the TEM images, by measuring the length of a line joining the midpoints of two parallel faces. The z lengths of NPc and NPrs were evaluated by electron tomography. Since the tilt-angle of the electron tomography sample-holder is limited (-70º to 70º), a direct measurement of the z length is not possible,[47] but can be estimated by the 3D reconstruction procedure performed with the softwares cited above. The z lengths of NPr and NPcs were estimated initially by taking TEM images of these particles tilted at high angles and using a geometric relation between x, y, z and the tilt angle. Afterwards, when the tomography of NPc and NPrs was performed, it was observed that this method underestimated the z length by around 15%, thus the z of NPcs and NPr were adjusted considering this difference. The 3D shape of NPr and NPcs could not be

evaluated with electron tomography due to the degradation of the sample after several measurements with an intense electron beam used to perform electron diffraction and high magnification imaging. The volume is deduced using the superquadrics model with the measured edge lengths Lx, Ly and Lz and the form factor n. n=2 for a sphere and tends to infinity for a rectangular parallelepiped.

2.3 Simulations

All FEM simulations described in the main text and the Supplementary Information were performed using the COMSOL commercial software. The vibrational simulations whose results are shown in **Figure S6** were done using the Structural Mechanics module of COMSOL. C_{11} = 191 GPa, C_{12} = 162 GPa, C_{44} = 42.4 GPa elastic parameters and 19283 kg/m³ density were used for gold. The data used as dielectric constant of gold is described in reference 48.[48] In these simulations, NPc shape was defined using a .stl file summarizing the results of its electron tomography characterization, and its vibrational eigenmodes were computed using stress-free boundary conditions on its surface. Calculations of the internal electric field distributions in cuboid nanoparticles (shown in Fig. 3) were performed using the Radio Frequency module of COMSOL. Illumination of the nanoparticles by a linearly polarised plane wave was considered in these simulations, and their inhomogeneous environment was explicitly included. A perfectly matched layer was defined at the border of the simulation domain to avoid spurious reflection effects.

Acoustic simulations involving more symmetric nanoparticle shapes allowing group-theory based discussions of the Raman activity of vibrational modes were done by considering superquadratic shapes defined by $|x/Lx|^n + |y/Ly|^n + |z/Lz|^n \leq 1$. The calculation of their vibrations was performed using the Rayleigh-Ritz variational approach, considering stress-free boundary conditions at the nanoparticle surface. For the cubic approximation, equal edge lengths ($Lx = Ly = Lz$) were considered, the form factor n being determined for each investigated nanoparticle from the ratio of the lengths along the [110] and [100] directions in TEM images. For the orthorhombic approximation, the same n value was used with the measured values of Lx, Ly and Lz. The details of the method are given in reference 49.

3. Results and discussion

Figure 1 shows the complete morphological characterization of these four particles. NPc and NPcs are cubic-shaped with round corners and well-defined edges (Figure 1(b-c, d)), whereas NPr and NPrs are closer to a spherical shape (Figure 1(a, e-f)). All nanoparticles are monocrystalline (see diffraction patterns in Supp. Information).

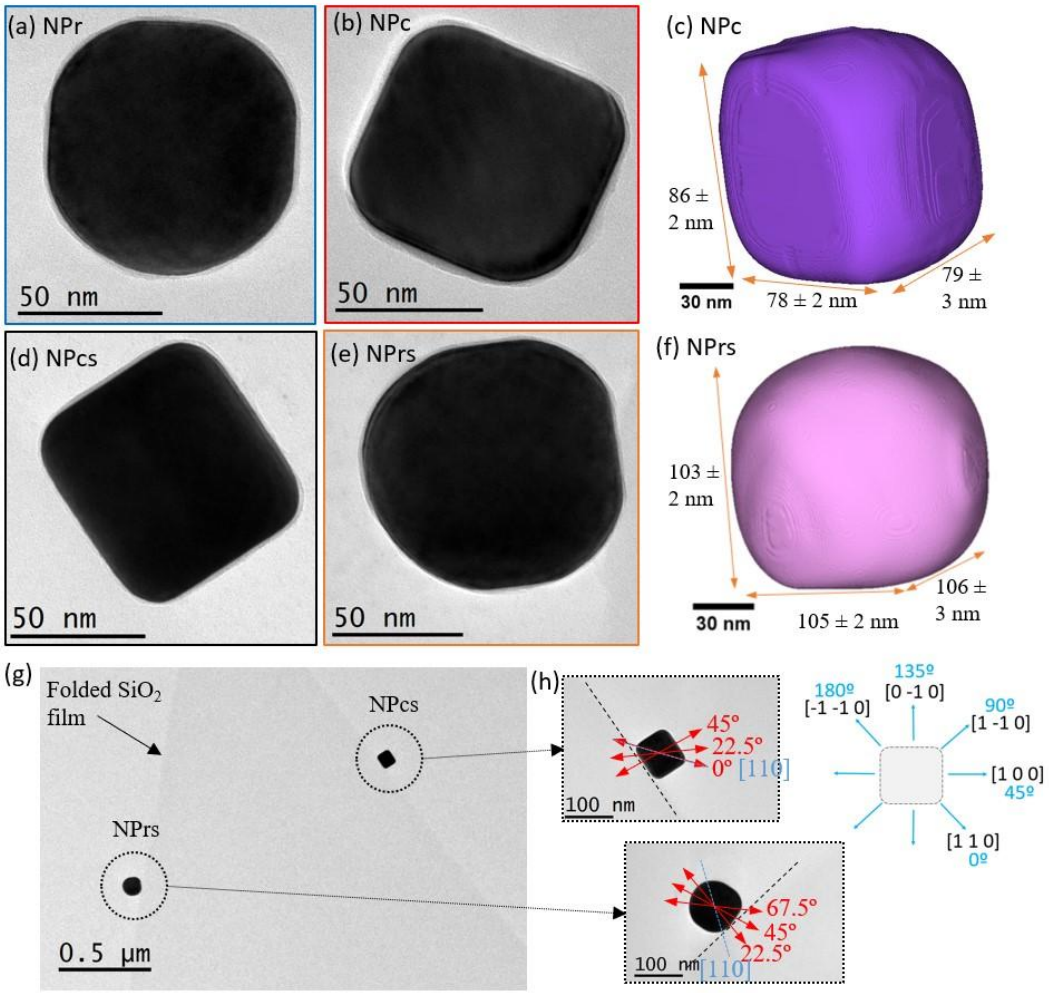

Figure 1. (a) Bright-field TEM image of NPr, (b) NPc, and (c) 3D model of NPc. (d) Bright-field TEM image of NPcs, (e) NPrs and (f) 3D model of NPrs. TEM images show that the particles are surrounded by a PVP layer of less than 2 nm thickness. (g) Low-magnification TEM image of the region in which NPcs and NPrs are located, where the SiO_2 film is folded. (h) Magnified images of NPcs and NPrs, showing the relation between particle position and polarization angles (red arrows). The dash-dotted lines represent the folded SiO_2 film. A scheme shows the relationship between the polarisation angles (blue) and the crystallographic directions of an Au particle in the Fm-3m space group (225).

The morphological parameters deduced from the TEM micrographs and considered in the numerical simulations for each nanoparticle (edge lengths Lx, Ly and Lz, and form factor n, determined from the ratio of the nanoparticle lengths along the [110] and [100] directions and quantifying its curvature) are listed in Table 1. The volume of each nanoparticle was

deduced from its estimated Lx, Ly and Lz and n values, assuming a superquadratic shape (see the Methods part).[49] A single characteristic length was deduced for each investigated nanoparticle by taking the cube root of its estimated volume. These characteristic lengths were used to normalize the vibrational frequencies measured for the four nanoparticles considered in this work (velocities expected to be size-independent being obtained by multiplying frequencies with the characteristic length) in order to more easily compare their vibrational spectra.

Table 1: Nanoparticle size values, characteristic lengths and form factors

Particle	**Edge length (nm)**			**Form factor n**	**Volume$^{1/3}$ (nm)**
	Lx	Ly	Lz		
NPr	84 ± 2	88 ± 2	85 ± 3	2.3	72 ± 2
NPc	78 ± 2	86 ± 2	79 ± 3	4.7	77 ± 3
NPcs	75 ± 2	80 ± 2	76 ± 3	4.6	73 ± 2
NPrs	105 ± 2	103 ± 2	106 ± 3	2.2	87 ± 3

Figure 2 shows the inelastic light scattering spectra of NPr and NPc obtained for an incident light polarisation angle of 0º, *i.e.* parallel to the crystallographic direction [110], together with the normalised frequencies of the acoustic modes computed for different shapes ranging from a spherical to an orthorhombic one (simulations based on the shape of NPc estimated by electron tomography being also presented in the Supplementary Information). As no significant change in the inelastic signal with varying polarisation was detected for NPr and NPc, only the spectra obtained at a polarisation angle of 0º are depicted in Figure 2(a-b) (measurements with other polarizations being shown in Figure 3).

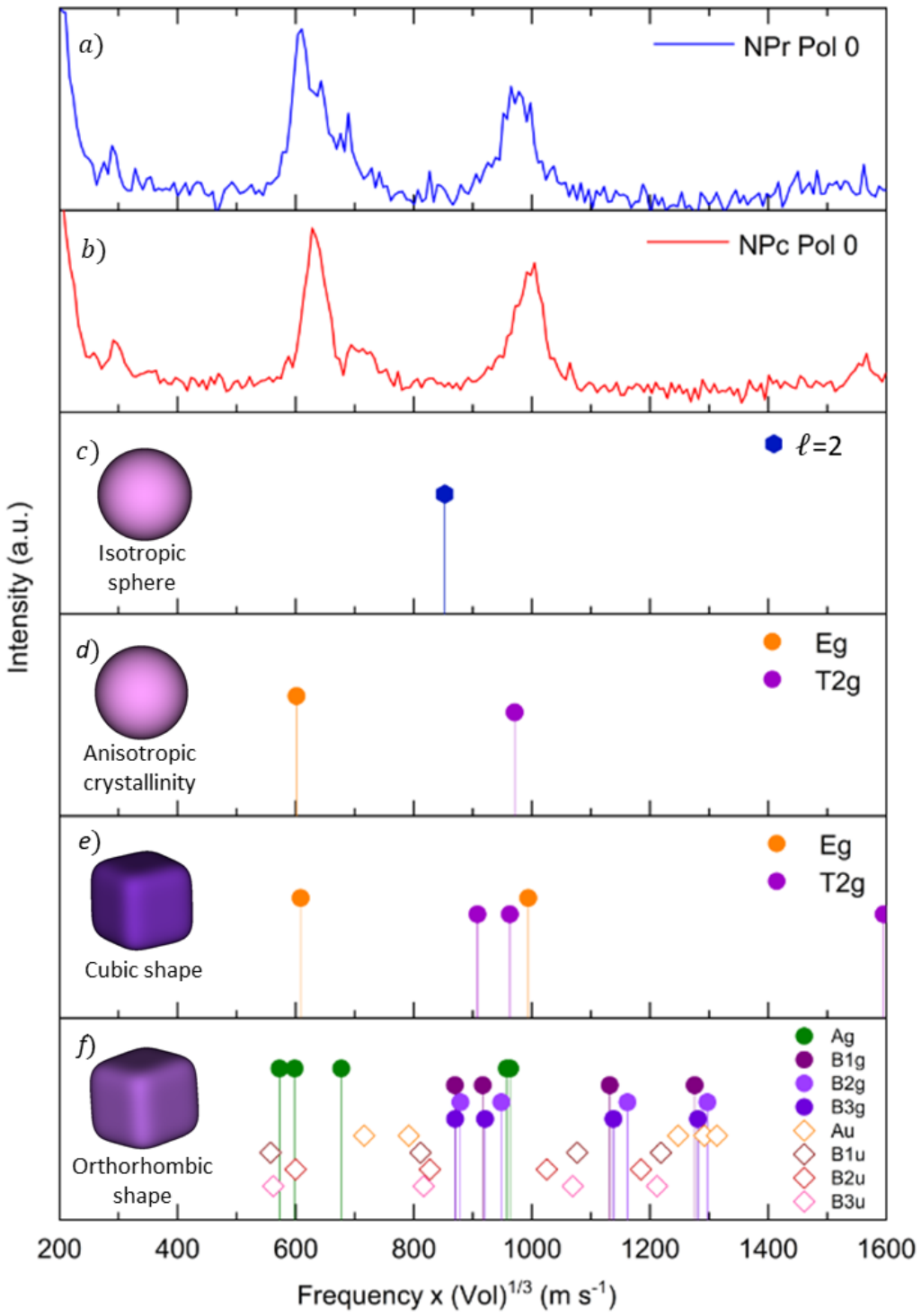

Figure 2. Low-frequency inelastic light scattering spectra of (a) NPr and (b) NPc measured with incident light polarised at 0º (along the crystallographic direction [110]). Expected Raman-active vibrational modes of (c) an elastically isotropic gold sphere, (d) an elastically anisotropic gold sphere, and (e) an elastically anisotropic gold cube. (f) Vibrational modes calculated considering a cuboid of lengths $x \neq y \neq z$ (orthorhombic symmetry). The irreducible representation of the modes is indicated; the solid and hollow symbols respectively represent the modes predicted to be Raman-active and non-Raman-active by usual selection rules, respectively, for the orthorhombic symmetry case. The values of x, y, and z are those obtained for the reconstructed form of NPc (see

Table 1). All frequencies were normalized by multiplying them by the cube root of the volume (characteristic length) of each particle, resulting in an x-axis expressed in velocity unit (m/s).

The experimental spectra measured on NPr and NPc show close similarities, with two main bands in each case, centered at velocities about 615 and 970 m/s for NPr and 630 and 1000 m/s for NPc. These observations are in good agreement with theoretical predictions for monocrystalline gold nanospheres and nanocubes. Indeed, for nanospheres, two Raman-active modes with a frequency ratio of about 1.5 are predicted by selection rules in the spectral range of the experiments, namely the acoustic modes E_g and T_{2g} resulting from the crystallinity-induced splitting of the l =2 mode of an isotropic sphere (Figure 2(c-d)). This splitting has already been observed in the case of assemblies of monocrystalline spherical gold nanoparticles.[41] When the shape of a crystalline nanoparticle changes from a sphere to a cube of similar characteristic length, the l =2 mode also splits into the E_g and T_{2g} modes (Figure 2(e)).

Apart from these main features, which are well explained by the consideration of perfect and highly symmetrical nanoparticle shapes (nanospheres and nanocubes) in the analysis, the spectra measured on NPr and NPc also present substructures never observed before in ensemble measurements. In the case of NPr, the lowest frequency peak is in fact made up of three distinct and partially overlapping peaks, while for NPc an additional low-amplitude peak is observable at 710 m/s. The observation of additional spectral features as compared to those predicted by the usual Raman selection rules for nanospheres and nanocubes is not surprising, considering that the nanoparticles investigated in this study are neither perfect nanocubes nor perfect nanospheres.

To investigate the effect of non-ideal nanoparticle morphologies, complementary numerical acoustic simulations were performed using an approach based on the description of the nanoparticles using an orthorhombic shape (associated with the D_{2h} point group and described with the superquadric model), accounting for the different x, y and z edge lengths of the investigated nanoparticles (Table 1), and thus representing a better approximation of the actual nanoparticle shapes than the cubic one. The reduced symmetry of the orthorhombic shape as compared to the cubic one lifts the degeneracy of some nanocube vibrational modes, which is required to assign the observed peaks, while still allowing the use of selection rules to predict Raman activities.

The frequencies calculated for orthorhombic symmetry allow us to assign to each mode an irreducible representation based on group theory (Figure 2(f)). Three Raman-active

A_g modes with close frequencies are predicted near 600 m/s instead of a single E_g mode in the cubic symmetry case, which provides a way to explain the experimental observations listed above. The two lower frequency A_g modes arise from the splitting of the cubic E_g vibration (degeneracy 2). The other A_g mode comes from a torsional mode of the sphere. It becomes Raman-active when the symmetry is lowered. Several Raman-active modes (with A_g, B_{1g}, B_{2g} and B_{3g} irreducible representations) are predicted near 1000 m/s, corresponding to the position of the second main experimental peak. They result from the splitting of the T_{2g} (degeneracy 3) and E_g cubic modes. It is difficult at this stage to assign the experimental peak to one of these modes, but we can point out that the calculated frequencies of the A_g modes are closer.

We also analyzed two other nanoparticles: NPcs, which is similar in size and shape to NPc (Figure 1(d)), and NPrs, which is similar in shape to NPr but larger (Figure 1(e-f)). NPcs and NPrs are located in a region of the sample where the SiO_2 film supporting the deposited nanoparticles is folded, forming a step right next to the particles (Figure 1(g)). Although such folding was not performed intentionally, it was very beneficial to this work as it allowed us to investigate how a strongly inhomogeneous environment affects inelastic light scattering by single nanoparticles.

Figure 3(a) and (b) show the low-frequency spectra of NPcs and NPrs as a function of incident polarisation. The spectra of NPc and NPr (presented in Figure 2 (a-b) in the case of 0° polarization angles), are also depicted in this figure, to facilitate comparison of the spectra measured with and without the silica step.

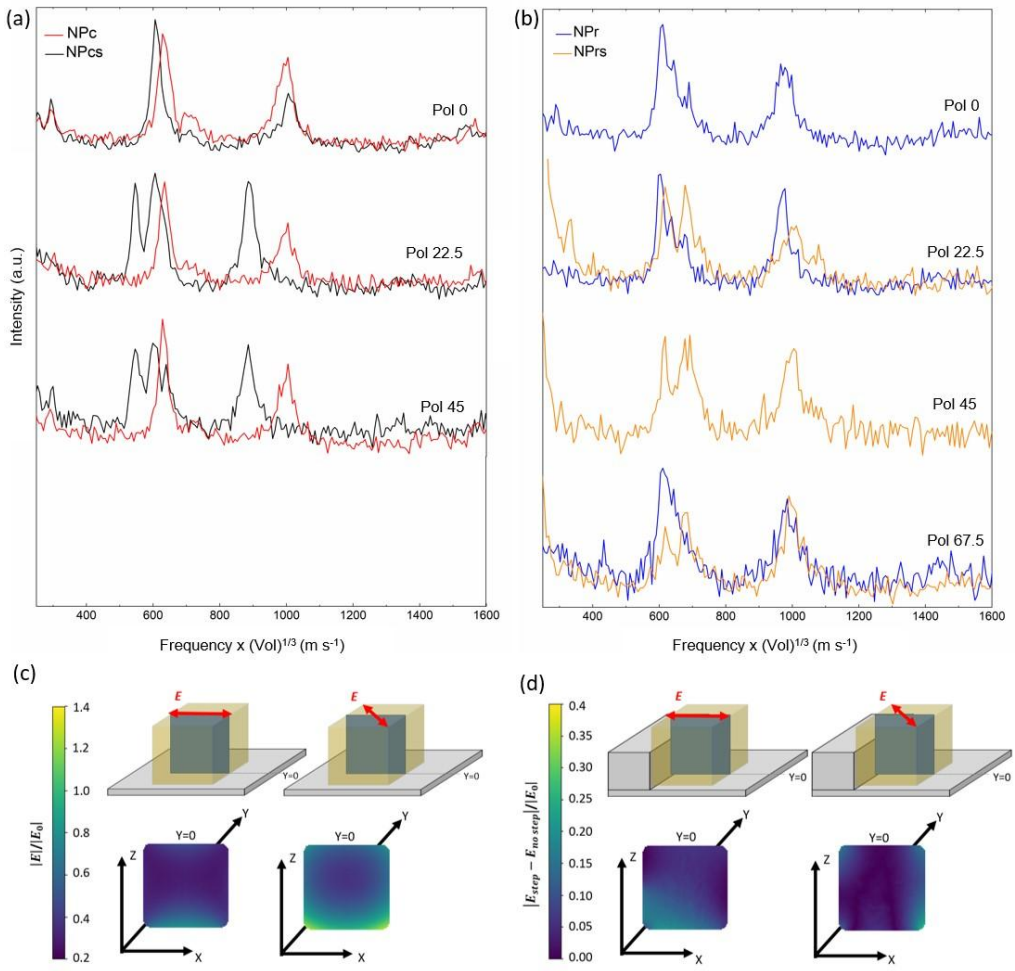

Figure 3. (a) Low-frequency inelastic scattering spectra of NPc and NPcs measured with incident light polarized at 0º, *i.e.*, along the crystallographic direction [110], 22.5º and 45º. (b) Low-frequency spectra of NPr and NPrs taken with incident light polarized at 0º, 22.5º, 45º, and -22.5º. (c) FEM-computed internal electric field of cuboid nanoparticles. This figure shows the internal electric field of a cuboidal Au particle deposited on a 40 nm thick SiO_2 substrate as a function of the polarisation direction. The simulations show cross-sectional views in the xz plane. (d) FEM-computed internal electric field distribution of a cuboid nanoparticle at the vicinity of a silica step. This image shows the absolute value of the difference between the internal electric field of an Au particle standing next to a 40 nm silica step and a particle where only the SiO_2 substrate is present. E_0 is the amplitude of the incident electric field. A superquadric shape, close to the shape estimated by EM tomography, was used for the calculation.

At a polarisation angle of 0º, the inelastic light scattering spectra measured for the cubic particles NPc and NPcs are very similar. The acoustic vibrational modes observed at 600 and 1000 m/s for NPcs are assigned as the peaks observed for NPc. However, when the polarisation angles are changed, the spectra of NPcs are strongly modified and differ significantly from those measured on NPc, which do not vary much with polarisation (Figure 3 (a)). Two peaks appear in the low-velocity range near 600 m/s, while at higher velocities a

peak at 880 m/s appears and the peak at 1000 m/s disappears. Usual selection rules predict that there are no Raman-active vibrations close to 600 m/s. The only other vibration modes in this frequency range come from the l=2 torsional mode of the sphere, which splits into B_{1u}, B_{2u} and B_{3u} modes for orthorhombic shape (Figure 2(g)). One possible explanation for the detection of such modes, predicted to be Raman-inactive by usual selection rules, is that the electric field distribution inside NPcs differs largely from the homogeneous one assumed to derive the selection rules, which are therefore probably not valid in this case.

A similar behaviour is observed for NPrs when compared to NPr. We observe that an additional mode appears in the low-velocity range for the considered polarization angles. The two low-frequency modes at 615 and 670 m/s can be assigned to the A_g and B_{3u} modes in the framework of orthorhombic shape models. In contrast to NPcs, in the high-velocity range, the mode at 1010 m/s (B_{1g}) is still observed but its intensity changes with varying polarisation.

For both NPcs and NPrs, modes that are not predicted to be Raman-active by usual selection rules for an orthorhombic shape are detected. Their appearance for NPcs and NPrs can be ascribed to the presence of the 40 nm SiO_2 step. The presence of this step can have two potential effects, as it can affect both the movement of the particles (mechanical effect) and the electric field distribution within them (optical effect). Although a mechanical effect of the silica step cannot be completely excluded, it is expected to be small as the nanoparticles used in this study are covered with a 2 nm polymer layer (Figure 1) that can act as a mechanical insulator between the cubes, the step, and the surface. Conversely, we have recently demonstrated that the internal electric field plays an important role in the Raman scattering cross-section of metal nanospheres.[17,36] One can thus expect that the detection of new modes in the presence of the step is related to the decrease of the symmetry of the internal electric field that it induces.

The modification of the inelastic response of NPcs as a function of polarization angle can be explained by considering the influence of the SiO_2 step on its internal electric field (Figure 3 (c) and (d)). When the polarisation becomes more parallel to the SiO_2 step (0º angle), an inelastic light scattering spectrum like the one obtained for NPc is obtained. In this case, optical FEM calculations predict no significant change of the internal electric field distribution compared to a supported particle. When the polarisation is perpendicular to the SiO_2 step, a strong modification of the inelastic response appears. In the case of NPrs, the three polarisation angles used for measurements correspond to directions more perpendicular to the step (see Figure 1(h)). As shown in Figure 3(d), with the presence of the step, the internal electric field of the particle becomes strongly asymmetric. The joint effects of the

SiO_2 substrate, step and the nanoparticle shape thus allow the observation of modes that are not usually active in Raman spectroscopy.

The modification of the internal electrical field due to the influence of the SiO_2 substrate could also contribute to the appearance of substructures in the low-frequency range for NPr and NPc. The SiO_2 substrate can change the symmetry of the electric field inside the particles, as only one face of the cuboid particle is in contact with the surface and hot spots can form near the edges of the cuboids. The electrical field distributions inside a cubic particle deposited on a 40 nm SiO_2 substrate were also calculated for polarisation angles of 0º (along the [110] direction) and 45º (along the face of the cube) and are depicted in Figure 3(c). A strong field gradient is indeed observed near the surface in contact with the substrate. This may be an additional factor favouring the appearance of additional peaks in the spectra.

4. Conclusion

In conclusion, the acoustic vibrations of single nanoparticles were studied by low-frequency Raman nano-spectrometry and the observed vibration modes were identified. Inelastic light scattering spectra composed of two main peaks were obtained and ascribed to a crystallinity-induced splitting of the quadrupolar mode usually dominating the Raman scattering spectra of spherical nanoparticles. Apart from this effect which had already been highlighted by previous experiments on assemblies of nanoparticles, our experimental spectra also presented subtler features associated to shape and environment effects. On the one hand, shape anisotropy (here associated to slightly different nanoparticle lengths along their three axes) was seen to induce additional degeneracy lifting of vibrational modes. On the other hand, the additional inhomogeneity of nanoparticle environment originating from the presence of a silica step at their vicinity was found to induce a polarisation-dependence of their inelastic scattering spectra and to allow the detection of modes predicted to be Raman-inactive by usual selection rules. This result was interpreted as the consequence of the modification of the distribution of the internal electric field by an inhomogeneous environment and opens the way to controlling the inelastic light scattering properties of nanoparticles by modification of their local environment. Even though only a limited number of particles and polarization angles could be investigated in this study due to the difficulty in controlling the positions of the particles and their surrounding environment, these results already show interesting features that were substantially supported by theoretical modelling. Although more quantitative models to account for the relation between the internal electric field of non-spherical nanoparticles and their inelastic light scattering spectra have yet to be

developed, this work demonstrates that it is possible to nano-engineer opto-acoustic properties at the scale of a single nanoparticle.

Supporting Information. Schematic representation of the experimental set-up and the steps of identification and localisation of the NPs with low-magnification TEM and confocal mapping images. Full (Stokes and anti-Stokes) low-frequency spectra of all particles, and detailed frequency values. Electron diffraction patterns of all particles, and FEM simulation example.

Acknowledgments. The authors acknowledge the Consortium Lyon Saint-Etienne de Microscopie (CLYM) for the access to the microscope. This work was funded by the ANR Project ANR-18-CE42-0009.

References

(1) Nasilowski, M.; Mahler, B.; Lhuillier, E.; Ithurria, S.; Dubertret, B. Two-Dimensional Colloidal Nanocrystals. *Chem. Rev.* **2016**, *116*, 10934–10982.

(2) Amendola, V.; Pilot, R.; Frasconi, M.; Maragò, O. M.; Iatì, M. A. Surface Plasmon Resonance in Gold Nanoparticles: A Review. *J. Phys. Condens. Matter* **2017**, *29*, 203002.

(3) Jain, P. K.; Huang, X.; El-Sayed, I. H.; El-Sayed, M. A. Review of Some Interesting Surface Plasmon Resonance-Enhanced Properties of Noble Metal Nanoparticles and Their Applications to Biosystems. *Plasmonics* **2007**, *2*, 107–118.

(4) Juodėnas, M.; Peckus, D.; Tamulevičius, T.; Yamauchi, Y.; Tamulevičius, S.; Henzie, J. Effect of Ag Nanocube Optomechanical Modes on Plasmonic Surface Lattice Resonances. *ACS Photonics* **2020**, *7*, 3130–3140.

(5) Roelli, P.; Galland, C.; Piro, N.; Kippenberg, T. J. Molecular Cavity Optomechanics as a Theory of Plasmon-Enhanced Raman Scattering. *Nat. Nanotechnol.* **2016**, *11*, 164–169.

(6) Cunha, J.; Guo, T. L.; Della Valle, G.; Koya, A. N.; Proietti Zaccaria, R.; Alabastri, A. Controlling Light, Heat, and Vibrations in Plasmonics and Phononics. *Adv. Opt. Mater.* **2020**, *8*, 2001225.

(7) Koya, A. N.; Cunha, J.; Guerrero-Becerra, K. A.; Garoli, D.; Wang, T.; Juodkazis, S.; Proietti Zaccaria, R. Plasmomechanical Systems: Principles and Applications. *Adv. Funct. Mater.* **2021**, *31* (2103706).

(8) Pan, H. H.; Wang, Z. K.; Lim, H. S.; Ng, S. C.; Zhang, V. L.; Kuok, M. H.; Tran, T. T.; Lu, X. M. Hypersonic Confined Eigenvibrations of Gold Nano-Octahedra. *Appl. Phys. Lett.* **2011**, *98* (13), 17–20.

(9) Pighini, C.; Aymes, D.; Millot, N.; Saviot, L. Low-Frequency Raman Characterization of Size-Controlled Anatase TiO2 Nanopowders Prepared by Continuous Hydrothermal Syntheses. *J. Nanoparticle Res.* **2007**, *9*, 309–315.

(10) Hodak, J. H.; Henglein, A.; Hartland, G. V. Size Dependent Properties of Au Particles : Coherent Excitation and Dephasing of Acoustic Vibrational Modes Size Dependent Properties of Au Particles : Coherent Excitation and Dephasing of Acoustic Vibrational Modes. *J. Chem. Phys.* **1999**, *111* (18), 8613–8621.

(11) Pelton, M.; Sader, J. E.; Burgin, J.; Liu, M.; Guyot-sionnest, P.; Gosztola, D. Damping of Acoustic Vibrations in Gold Nanoparticles. *Nat. Nanotechnol.* **2009**, *4*, 492–495.

(12) Hu, M.; Wang, X.; Hartland, G. V; Mulvaney, P.; Juste, J. P.; Sader, J. E. Vibrational Response of Nanorods to Ultrafast Laser Induced Heating : Theoretical and Experimental Analysis. *J. Am. Chem. Soc.* **2003**, *125*, 14925–14933.

(13) Del Fatti, N.; Voisin, C.; Chevy, F.; Vallée, F.; Flytzanis, C.; Flytzanis, C. Coherent Acoustic Mode Oscillation and Damping in Silver Nanoparticles. *J. Chem. Phys.* **1999**, *110* (23), 11484–11487.

(14) Portalès, H.; Goubet, N.; Saviot, L.; Yang, P.; Sirotkin, S.; Duval, E.; Mermet, A.; Pileni, M.-P. Crystallinity Dependence of the Plasmon Resonant Raman Scattering by Anisotropic Gold Nanocrystals. *ACS Nano* **2010**, *4* (6), 3489–3497.

(15) Yu, K.; Sader, J. E.; Zijlstra, P.; Hong, M.; Xu, Q. H.; Orrit, M. Probing Silver Deposition on Single Gold Nanorods by Their Acoustic Vibrations. *Nano Lett.* **2014**, *14* (2), 915–922.

(16) Mongin, D.; Juvé, V.; Maioli, P.; Crut, A.; Del Fatti, N.; Vallée, F.; Sánchez-Iglesias, A.; Pastoriza-Santos, I.; Liz-Marzán, L. M. Acoustic Vibrations of Metal-Dielectric Core-Shell Nanoparticles. *Nano Lett.* **2011**, *11*, 3016–3021.

(17) Girard, A.; Gehan, H.; Crut, A.; Mermet, A.; Saviot, L.; Margueritat, J. Mechanical Coupling in Gold Nanoparticles Supermolecules Revealed by Plasmon-Enhanced Ultralow Frequency Raman Spectroscopy. *Nano Lett.* **2016**, *16* (6), 3843–3849.

(18) Martinet, Q.; Baronnier, J.; Girard, A.; Albaret, T.; Saviot, L.; Mermet, A.; Abecassis, B.; Margueritat, J.; Mahler, B. Ligand-Dependent Nano-Mechanical Properties of CdSe Nanoplatelets: Calibrating Nanobalances for Ligand Affinity Monitoring. *Nanoscale* **2021**, *13*, 8639–8647.

(19) Crut, A.; Maioli, P.; Fatti, N. Del; Vallée, F. Acoustic Vibrations of Metal Nano-Objects : Time-Domain Investigations. *Phys. Rep.* **2015**, *549*, 1–43.

(20) Duval, E. Far-Infrared and Raman Vibrational Transitions of a Solid Sphere: Selection Rules. *Phys. Rev. B* **1992**, *46* (9), 5795–5797.

(21) Sinogeikin, S. V.; Lakshtanov, D. L.; Nicholas, J. D.; Bass, J. D. Sound Velocity Measurements on Laser-Heated MgO and Al2O3. *Phys. Earth Planet. Inter.* **2004**, *143* (1–2), 575–586.

(22) Li, Y.; Lim, H. S.; Ng, S. C.; Kuok, M. H.; Ge, M. Y.; Jiang, J. Z. Brillouin Study of Acoustic Phonon Confinement in GeO2 Nanocubes. *Appl. Phys. Lett.* **2007**, *91* (9), 2005–2008.

(23) Portales, H.; Saviot, L.; Duval, E.; Fujii, M.; Hayashi, S. Resonant Raman Scattering by Breathing Modes of Metal Nanoparticles. *J. Chem. Phys.* **2001**, *115* (8), 3444–3447.

(24) Saviot, L.; Champagnon, B.; Duval, E. Size-Selective Resonant Raman Scattering in CdS Doped Glasses. *Phys. Rev. B* **1998**, *57* (1), 341–346.

(25) Duval, E.; Boukenter, A.; Champagnon, B. Vibration Eigenmodes and Size of Microcrystallites in Glass : Observation by Very-Low-Frequency Raman Scattering. *Phys. Rev. Lett.* **1986**, *56* (19), 2052–2055.

(26) Boukenter, A.; Champagnon, B.; Duval, E.; Wright, A. Low-Frequency Raman Scattering in a Nucleate Cordierite Glass. *J. Phys. Colloq.* **1985**, *46 (C8)*, C8-443-C8-447.

(27) Lamb, H. On the Vibrations of an Elastic Sphere. *Proc. London Math. Soc.* **1881**, *s1-13*, 189–212.

(28) Juvé, V.; Crut, A.; Maioli, P.; Pellarin, M.; Broyer, M.; Del Fatti, N.; Vallée, F. Probing Elasticity at the Nanoscale: Terahertz Acoustic Vibration of Small Metal Nanoparticles. *Nano Lett.* **2010**, *10*, 1853–1858.

(29) Martinet, Q.; Berthelot, A.; Girard, A.; Donoeva, B.; Comby-Zerbino, C.; Romeo, E.; Bertorelle, F.; Van Der Linden, M.; Tarrat, N.; Combe, N.; et al. Performances of the Lamb Model to Describe the Vibrations of Gold Quantum-Sized Clusters. *J. Phys. Chem. C* **2020**, *124*, 19324–19332.

(30) Saviot, L.; Mermet, A.; Duval, E. Acoustic Vibrations in Nanoparticles. In *Handbook of Nanophysics: Nanoparticles and Quantum Dots*; Sattler, K. D., Ed.; Taylor & Francis Group, 2010; pp 11.1-11.17.

(31) Crut, A.; Juvé, V.; Mongin, D.; Maioli, P.; Del Fatti, N.; Vallée, F. Vibrations of Spherical Core-Shell Nanoparticles. *Phys. Rev. B - Condens. Matter Mater. Phys.* **2011**, *83* (205030), 1–9.

(32) Margueritat, J.; Gonzalo, J.; Afonso, C. N.; Sabatier, P.; Narbonne, D.; Cedex, T.; Murray, D. B.; Saviot, L. Surface Plasmons and Vibrations of Self-Assembled Silver Nanocolumns. *Nano Lett.* **2006**, *6* (9), 2037–2042.

(33) Portales, H.; Goubet, N.; Saviot, L.; Adichtchev, S.; Murray, D. B.; Mermet, A.; Duval, E.; Pileni, M. Probing Atomic Ordering and Multiple Twinning in Metal Nanocrystals through Their Vibrations. *PNAS* **2008**, *105* (39).

(34) Girard, A.; Lermé, J.; Gehan, H.; Mermet, A.; Bonnet, C.; Cottancin, E.; Crut, A.; Margueritat, J. Inelastic Light Scattering by Multiple Vibrational Modes in Individual Gold Nanodimers. *J. Phys. Chem. C* **2019**, *123* (23), 14834–14841.

(35) Girard, A.; Lermé, J.; Gehan, H.; Margueritat, J.; Mermet, A. Mechanisms of Resonant Low Frequency Raman Scattering from Metallic Nanoparticle Lamb Modes. *J. Chem. Phys.* **2017**, *146*, 194201.

(36) Girard, A.; Gehan, H.; Mermet, A.; Bonnet, C.; Lermé, J.; Berthelot, A.; Cottancin, E.; Crut, A.; Margueritat, J. Acoustic Mode Hybridization in a Single Dimer of Gold Nanoparticles. *Nano Lett.* **2018**, *18* (6), 3800–3806.

(37) Dijk, M. A. Van; Lippitz, M.; Orrit, M. Detection of Acoustic Oscillations of Single Gold Nanospheres by Time-Resolved Interferometry. *Phys. Rev. Lett.* **2005**, *267406*

(December), 1–4.

(38) Staleva, H.; Hartland, G. V. Transient Absorption Studies of Single Silver Nanocubes. *J. Chem. C* **2008**, *112*, 7535–7539.

(39) Medeghini, F.; Crut, A.; Gandolfi, M.; Rossella, F.; Maioli, P.; Vallée, F.; Banfi, F.; Del Fatti, N. Controlling the Quality Factor of a Single Acoustic Nanoresonator by Tuning Its Morphology. *Nano Lett.* **2018**, *18*, 5159–5166.

(40) Hörl, A.; Haberfehlner, G.; Trügler, A.; Hohenester, U.; Kothleitner, G. Tomographic Imaging of the Photonic Environment of Plasmonic Nanoparticles. *Nat. Commun.* **2017**, *8* (37), 1–6.

(41) Li, X.; Haberfehlner, G.; Hohenester, U.; Kothleitner, G.; Kociak, M. Three-Dimensional Vectorial Imaging of Surface Phonon Polaritons. **2021**, *1367* (March), 1364–1367.

(42) Kremer, J. R.; Mastronarde, D. N.; McIntosh, J. R. Computer Visualization of Three-Dimensional Image Data Using IMOD. *J. Struct. Biol.* **1996**, *116*, 71–76.

(43) Gordon, R.; Bender, R.; Herman, G. T. Algebraic Reconstruction Techniques (ART) for Three-Dimensional Electron Microscopy and X-Ray Photography. *J. Theor. Biol.* **1970**, *29*, 471–481.

(44) Messaoudil, C.; Boudier, T.; Sorzano, C. O. S.; Marco, S. TomoJ: Tomography Software for Three-Dimensional Reconstruction in Transmission Electron Microscopy. *BMC Bioinformatics* **2007**, *8* (288), 1–9.

(45) Arganda-Carreras, I.; Fernández-González, R.; Muñoz-Barrutia, A.; Ortiz-De-Solorzano, C. 3D Reconstruction of Histological Sections: Application to Mammary Gland Tissue. *Microsc. Res. Tech.* **2010**, *73*, 1019–1029.

(46) Fedorov, A.; Beichel, R.; Kalpathy-Cramer, J.; Finet, J.; Fillion-Robin, J. C.; Pujol, S.; Bauer, C.; Jennings, D.; Fennessy, F.; Sonka, M.; et al. 3D Slicer as an Image Computing Platform for the Quantitative Imaging Network. *Magn. Reson. Imaging* **2012**, *30*, 1323–1341.

(47) Ercius, P.; Alaidi, O.; Rames, M. J.; Ren, G. Electron Tomography: A Three-Dimensional Analytic Tool for Hard and Soft Materials Research. *Adv. Mater.* **2015**, *27* (38), 5638–5663.

(48) P. B. Johnson and R. W. Christy. Optical Constant of the Nobel Metals. *Phys. Rev. B* **1972**, *6* (12), 4370–4379.

(49) Saviot, L. Free Vibrations of Anisotropic Nano-Objects with Rounded or Sharp Corners. *Nanomaterials* **2021**, *11*, 1838.

TOC Graphic